Magnetic-Assisted Transparent and Flexible Percolative Composite for Highly Sensitive Piezoresistive Sensor via Hot Embossing Technology

Shan Wang,[†] Guorui Chen,[†] Shaoyu Niu,[†] Kaifeng Chen,[†] Tian Gan,[†] Zongrong Wang,[*,†] Hongzhu Wang,[*,‡] Piyi Du,[†] Chi Wah Leung,[*,//] and Shaoxing Qu[*,§]

† State Key Lab of Silicon Materials, School of Materials Science and Engineering, ‡ Department of Equipment Division, Women's Hospital, School of Medicine, and § State Key Laboratory of Fluid Power & Mechatronic System, Key Laboratory of Soft Machines and Smart Devices of Zhejiang Province, Center for X-Mechanics, and Department of Engineering Mechanics, Zhejiang University, Hangzhou 310027, China // Department of Applied Physics, The Hong Kong Polytechnic University, Hung Hom, Hong Kong 999077, China

Abstract:

A highly transparent and flexible percolative composite with magnetic reduced graphene oxide@nickel nanowire (mGN) fillers in EcoFlex matrix is proposed as a sensing layer to fabricate high-performance flexible piezoresistive sensors. Large excluded volume and alignment of mGN fillers contribute to low percolation threshold (0.27 vol %) of mGN-EcoFlex composites, leading to high electrical conductivity of 0.003 S m^{-1}, optical transmittance of 71.8%, and low Young's modulus of 122.8 kPa. Large-scale microdome templates for sensors are prepared by hot embossing technology cost-effectively and COMSOL Multiphysics is utilized to optimize the sensor performances. Piezoresistive sensors fabricated experimentally show superior average sensitivity of 1302.1 kPa^{-1} with a low device-to-device variation of 3.74%, which provides a new way to achieve transparent, highly sensitive, and large-scale electronic skin.

Keywords:

hot embossing, percolative composite, excluded volume, transparent, piezoresistive sensors

Introduction

Flexible electronics, especially pressure sensor, is an emerging area in recent years and has attracted wide interests for the vast promising applications, such as flexible display, soft robotics, human motion monitoring, electronic skins (e-skin), and health care. (1−4) Just like the mechanoreceptors of human skins, with the capability of real-time tracking physiological signals, including temperature, (1,5) pressure, (2,6−8) strain, (3,9−12) humidity, (13) etc, flexible sensors are crucial components in e-skin. High sensitivity, optical transparency, fast response, and long-term stability are all essential for high-performance pressure sensors of wearable electronics. Most of the pressure sensors reported till now are composed of surface conducting layer, such as poly(3,4-ethylenedioxythiophene):poly(styrenesulfonate) (PEDOT:PSS), (14,15) reduced graphene oxide (rGO), (16,17) single-wall carbon nanotubes (SWCNTs), (1,18) and metallic nanomaterials, (19,20) coated on top of microstructured deforming layer like poly(dimethylsiloxane) (PDMS). However, owing to Young's modulus mismatch between deforming layer of PDMS (∼2.5 MPa) and the conducting layer (for instance, Young's modulus of PEDOT:PSS is around 2.5 GPa), cracks or even detachment have been reported to occur after thousands of loading and unloading cycles, (21,22) which will cause stability issue due to cracks, detachment, or other failures.

In this regard, how to avoid the mismatch between the deforming and the conducting materials is the key to assure the sensor stability. Actually, it is difficult to find two materials with perfectly matching properties. Hence, if one material with both high conductivity and low Young's modulus could be developed to replace the two-layer structure, then the mismatch problem could be addressed. Here, a percolative conductive composite film with low Young's modulus has been proposed as the sensing layer to provide an alternative solution for replacing the traditional two-layer structure.

When the insulating polymer matrix is filled with a certain content of electrically conductive fillers, the composite will transform from insulator to conductor and this

critical volume ratio is called the percolation threshold according to the percolation theory. (23,24) The percolation threshold is affected by the size, shape, distribution, and alignment of fillers in the matrix. For spherical fillers, the percolation threshold could be high as 12–16%, and even for one-dimensional filler with high aspect ratio, this value is still around 3%. (23,25−27) The high content of fillers will dramatically reinforce the composite owing to their high strength and stiffness. (28,29) Furthermore, most of the opaque fillers will also affect the transmittance of the composite and limit the application in certain fields. (30,31)

In this case, to achieve high electrical conductivity, low Young's modulus, high optical transparency, and cost-effectiveness at the same time, a lower volume ratio of the conductive filler is highly preferred. Hence, fillers with large excluded volume that would contribute to a low percolation threshold are desirable. (32−34) Besides, the alignment of fillers by a magnetic or electric field would decrease the percolation threshold further to achieve the requirements above.

Last but not least, large-area production, reproducibility, and low cost are all very important factors for the wide application of e-skin. (14,15,19,35) Nevertheless, many pressure sensors are molded from microstructured templates that largely depend on the traditional lithography technique, which is both time and cost consuming. (14,35) Although many reports have proposed some templates that are promising in producing large scale and inexpensive pressure sensors, such as mimosa (19) and sandpaper, (15) the reproducibility and stability of sensors are still limited by the intrinsic characteristics of these templates and needed to be enhanced.

Herein, hybrids of magnetic rGO@nickel nanowires (NiNWs), denoted as mGN hybrids, were synthesized with large excluded volume and controllable alignment by magnetic field, which resulted in a lower percolation threshold of mGN-EcoFlex composite that is electrically conductive, optically transparent, and of low Young's modulus. The conductive composite was applied as the sensing layer to replace the traditional two-layer structure and contributed to high-performance piezoresistive sensor. From the perspective of microstructures, hot embossing technology was used

to fabricate the micro-dome templates with both controllable diameter and height, which is simple, cost-effective, and capable of large-scale production. The proposed magnetic-assisted piezoresistive sensor exhibits high sensitivity, transparency, repeatability, and stability, providing a new way to realize transparent, highly sensitive, and large-scale e-skin for applications like health monitoring, soft robotics, etc.

Results and Discussion

Figure 1a shows the schematic formation mechanism of mGN hybrids. Graphene oxide (GO) is negatively charged owing to the existence of oxygen-containing functional groups such as hydroxyl, epoxide, and carboxyl groups and could be dispersed uniformly in water. (36) After mixed with hydrazine hydrate, the nickel oxide layer of NiNWs would react with N2H4 to form [Ni(NH3)2]2+, which could be captured by GO sheets via electrostatic attraction. (37) Then, during the formation of Ni0 from [Ni(NH3)2]2+, GO is simultaneously reduced to rGO by hydrazine hydrate. At the same time, NiNWs would be attached to the surface of rGO and form mGN hybrids, as shown in Figure 1a. The transmission electron microscopy (TEM) images of Figure 1b,c show that both GO sheets and the synthesized NiNWs possess a large length width (L/W) ratio. The TEM and scanning electron microscopy (SEM) images of mGN hybrids are displayed in Figure 1d,e, which show that rGO sheets were decorated with NiNWs and connected with each other (Figure S1). This makes it possible to manipulate the orientation of mGN hybrids by an external magnetic field through the magnetism of NiNWs.

As shown in the XRD patterns of Figure 1f, GO exhibits a peak at $2\theta = 11°$ that corresponds to the interlayer distance of 0.8 nm, which is larger than the interlayer distance of graphite (0.34 nm), revealing that many different oxygen-containing groups might have been intercalated into the interlayer space. (37) The characteristic peak at $2\theta = 24°$ of rGO implies that GO has been reduced to rGO. The peaks at 44.7, 52.0, and 76.6° in NiNWs and mGN hybrids correspond to the (111), (200), and (220) crystal planes of Ni, which match the face-centered cubic Ni [JCPDS 04-0850, space

group, Fm3m (225)].

The reduction of GO to rGO and the formation of mGN hybrids could also be verified by Fourier transform infrared (FTIR) spectroscopy analysis. As shown in Figure 1g, many characteristic bands appear in the spectrum of GO, which corresponds to different oxygen-containing functional groups. The bands at 1060, 1220, and 1730 cm−1 correspond to C−O, C−O−C, and C═O stretching vibrations. The bands at 1620 and 3400 cm−1 are ascribed to O−H stretching vibrations. But in mGN hybrids, most of the absorption peaks are weakened or even disappear, indicating the removal of corresponding oxygen-containing groups after the reduction of GO to rGO and the formation of mGN. (38)

Raman spectra were used to further confirm the formation of mGN hybrids and Figure 1h exhibits the Raman scattering signals of GO, rGO, and mGN hybrids, respectively. The spectra show two distinct peaks near 1350 and 1580 cm−1, corresponding to the D band and G band, respectively. The D band results from the disordered carbon atoms, whereas the G band comes from sp2 bonded carbon atoms. The intensity ratio of ID/IG is generally used to evaluate the crystal structural disorder of graphene. The higher the ratio of ID/IG, the higher the disorder degree. (39) As shown in Figure 1h, ID/IG slightly increases from 0.91 to 1.12 after the reduction of GO to rGO. And the disorder increase may be ascribed to the smaller size of reestablished aromatic domains, (40) which indicated that oxide functional groups on the GO surface were reduced and large quantity of structural defects were formed. (41) However, after the formation of the mGN hybrids, ID/IG decreases a little again to 0.98 because of the attachment of NiNWs to rGO sheets.

Transparent mGN-EcoFlex Conductive Film

As discussed above, to achieve high electrical conductivity, high optical transparency, and at the same time preserving the low Young's modulus of polymer matrix, a low percolation threshold of the composite is extremely important. Excluded volume theory is the most widely used model to study the influences of filler morphology on

percolation threshold, where excluded volume is the volume around the object into which another identical object cannot enter without contacting the first object. A two-dimensional (2D) schematic illustration of the excluded area was used to explain excluded volume theory, as shown in Figure 2a. The total area of 50 spheres in Figure 2a-i is approximately equal to the area of seven rods in Figure 2a-ii, indicating that the area ratios are the same. As shown in Figure 2a-i, 50 spheres take up some area (black) in the square and plenty of room (white) is still left for other spheres to occupy, thus leads to very small excluded area (purple). However, as shown in Figure 2a-ii, there is a much larger area in the system that other rods cannot occupy although the total area of seven rods is the same as that of 50 spheres. Therefore, the excluded area of the system with rods as filler is larger than the one with spheres. It can be seen that there is no conductive path of the sphere system in Figure 2a-i but a conductive network of rods has already formed in Figure 2a-ii with the same area ratio. Therefore, with the same filler content, fillers with larger excluded volume would form conductive networks more easily, thus contributing to a lower percolation threshold, as shown in Figure 2b. (32−34,42)

The average excluded volume (Vex) of randomly oriented spheres, (32) rods, (34) and thin disks (33) are

$$V_{ex}^{s} = \left(\frac{2\pi}{3}\right)D_s^3 \tag{1}$$

$$V_{ex}^{r} = \left(\frac{\pi}{2}\right)L_r^2 D_r + 2\pi D_r^2 L_r + \left(\frac{4}{3}\right)\pi D_r^3 \tag{2}$$

$$V_{ex}^{d} = \left(\frac{\pi^2}{8}\right)D_d^3 \tag{3}$$

where the superscripts s, r, d stand for spheres, rods, and disks, respectively. Ds is the diameter of spheres. Lr and Dr are the length and diameter of rods, respectively. Dd is the diameter or lateral size of disks. Divide eq 2 by eq 1, eq 3 by eq 1, the excluded volume ratios of rod to sphere and disk to sphere are obtained as eqs 4 and 5 below

$$\frac{V_{ex}^{r}}{V_{ex}^{s}} = \frac{3}{4}\left(\frac{L_r}{D_s}\right)^2 \tag{4}$$

$$\frac{V_{ex}^{d}}{V_{ex}^{s}} = \frac{3\pi}{16}\left(\frac{D_d}{D_s}\right)^3 \quad (5)$$

From eq 4, NiNWs with a length of about tens of micrometers show excluded volume several orders of magnitude higher than that of the ordinary sphere fillers with a diameter of about tens of nanometers. From eq 5, rGO sheets in this study possess a large lateral size of several microns, much higher than the diameter of the sphere, leading to the superior high excluded volume. Therefore, mGN fillers with large L/W ratios could exhibit very high excluded volumes, which are easy to form a conductive network and thus realize a very low percolation threshold of the mGN-EcoFlex film.

In addition, a controlled orientation of fillers by electric or magnetic fields can help to form conductive paths easily in the alignment direction, thus resulting in a relative low percolation threshold. (23,25,43,44) The alignment of mGN fillers could be manipulated by a magnetic field when curing owing to the magnetic dipole interaction (Figure S2). (45,46)

As shown in Figure 2c, for the films with random mGN fillers, it is not conductive with volume ratios below 1.0 vol % because the content of mGN fillers is not enough to form a percolation conductive network. However, the threshold of films with vertically aligned mGN fillers is low as 0.27 vol % with a conductivity of 0.003 S m–1 since the vertically aligned mGN fillers are easier to form continuous conductive pathways in the z direction. In other words, with the same content of fillers, the conductivity of vertical films is higher than that of random films, revealing that orientation of mGN fillers inside the polymer matrix improves the conductivity of composites in the alignment direction and as a result greatly decreases the percolation threshold.

In addition to the increase in conductivity, the alignment of mGN fillers could also improve the transmittance of mGN-EcoFlex films, which is important in certain applications requiring transparent e-skins. As shown in Figure 2d, with mGN fillers aligned vertically to the x–y plane, the lights along the z axis could pass through the

film with being scattered a lot less than the film with mGN fillers aligned randomly, increasing the transmittance of the mGN-EcoFlex composites. From Figure 2e, the vertical film with even 1.0% of mGN fillers is transparent enough to make the letters behind clearly observed. Figure 2f shows the transmittances of films with different mGN volume ratios and alignment directions. It is seen that the transmittances of films with vertical mGN fillers are much higher than those of films with random mGN fillers at the same content of mGN hybrids, which proved that the transparency of films could be improved obviously by the alignment of fillers.

Figure 2g presents the relationships among conductivity, transmittance, Young's modulus, and the volume ratio of fillers in the films, which indicate that the conductivity increases but transmittance decreases as the loading of mGN increases. However, the film is still both electrically conductive and optically transparent when the volume ratio is between 0.27 and 1.0 vol %. Besides, Young's modulus of films slightly increases with the content increase of mGN owing to the reinforcement effect of fillers. However, mGN-EcoFlex composites show low Young's modulus from 101.6 kPa (0.15% mGN) to 156.1 kPa (4.0% mGN), which is still close to the value of pure EcoFlex film of 81.0 kPa and human skins of 41–1950 kPa. (47,48) Therefore, a low loading of mGN fillers would preserve the low Young's modulus of a polymer matrix, and realize both high electric conductivity as well as optical transparency at the same time, making it appropriate for the sensing layer of a piezoresistive sensor to replace the traditional two-layer structure.

Fabrication of Magnetic-Assisted Piezoresistive Sensor

The flow chart of preparation of micro-dome templates by hot embossing technology and micro-patterned mGN-EcoFlex film derived from the template is shown in Figure 3a. The morphologies of the film molded from template prepared at a hot embossing pressure of 60 kPa under 130 °C are shown in Figure 3b–d. As shown in Figure 3b, the micro-domes dispersed densely and uniformly on the polycarbonate substrate with a diameter of about 30 μm. One single micro-dome was characterized by three-dimensional (3D) optical microscope (OM) from the perspective (Figure 3c) and

top view (Figure 3d), which exhibits an average height of 13.43 μm, close to the radius of SiO2 microspheres. To prepare the magnetic-assisted piezoresistive sensor, 1.0 vol % of mGN fillers are mixed with EcoFlex using the prepared template. The magnetic fillers are then aligned vertically to the x–y plane by an external magnetic field during curing, as shown in Figure 3a,e.

Theoretically, the number of micro-domes has a great influence on the sensor performances, which could be controlled by the hot embossing pressure while preparing templates. To provide detailed guidance for template preparation, COMSOL Multiphysics was used to figure out the influences of micro-domes density and height on sensor performances. The simulation of the sensor under continuous loading was conducted in the alternating current (AC)/direct current (DC) module using a stationary solver of COMSOL Multiphysics 5.3. Two in-plane electrodes were constructed. One was grounded and another was biased with 1 V. A cuboid block in size of 500 μm × 360 μm × 80 μm (weight × length × height) was combined with micro-dome array by Boolean operations. Then, the bottom textured side was in contact with electrodes and the continuous force was applied on the surface of the top flat side with an area of 500 μm × 360 μm, resulting in the change of contact area between the microstructures and electrodes, and thus causing the resistance change of the sensor correspondingly. To mimic the real situation during template preparation that higher hot embossing pressure would increase both the density and height of dome all the way to hemisphere, pressure sensors with increasing micro-dome density of 24, 36 and 48% and height of 14, 24 and 34 μm were built in COMSOL, respectively, as shown in Figure 3f. Continuous loading was applied to the surface of sensors with different densities and the current change was recorded, as shown in Figure 3g. It can be seen that the higher the density, the higher the sensitivity of sensors. Because the higher density of micro-domes would lead to more contact points with an electrode, which increases the change of total contact area and the contact resistance under the same external pressure, thus improving the sensitivity of the pressure sensor. Besides, the deformation of the sensor with a larger height of

micro-domes would be easier and larger than that with small height, which contributes to a significant change in contact area and thus higher sensitivity.

Based on the COMSOL simulation result that the sensitivity of pressure sensor increases as the density and height of micro-domes, a series of hot embossing pressures, including 12, 18, 38, and 60 kPa, were applied to acquire templates with different densities and heights of micro-domes. SEM was used to analyze the morphologies of mGN-EcoFlex films molded from the templates prepared at different hot embossing pressures (Figure S3a–d). The density and diameter of micro-domes increase as the hot embossing pressure increases, which contributes to a large change of contact area and thus high sensitivity of the sensor (Figure S3e).

Apart from the contribution of micro-dome deformation to the sensor sensitivity, the change of tunneling current under external pressure would also play a significant role in sensor piezoresistivity. Some fillers might touch each other and some others are separated by polymer matrix between adjacent fillers owing to the low volume ratio of fillers in the mGN/EcoFlex composite. Under pressure, mGN fillers become closer to the order of tunneling distance and carriers will transport from one particle to another more easily, thus forming tunneling current even when they do not touch geometrically. On the other hand, the contact area of the existing contacted fillers would also increase, leading to the resistance change of the sensor. Thus, the sensor resistance decreases with the increase in pressure and realize the piezoresistivity. (42,44,49−51)

To confirm the influences of mGN alignment and device microstructure on the sensor performance, devices with vertically aligned mGN and micro-domes structure, with randomly distributed mGN and micro-domes structure, with vertically aligned mGN and planar structure were fabricated, which are denoted as vertical & micro-domes, random & micro-domes, and vertical & planar, respectively.

Figure 4a plots the representative current response curves (the average of four response curves, Figure S4) of three sensors with different alignment and

microstructure loaded by a force gauge (Figure 4e). Continuous loadings generated by the force gauge were applied to the sensor through a silicon wafer with an area of 5 mm × 5 mm. The current signals were measured and recorded by a LabVIEW-controlled Keithley 2602 source meter under a bias voltage of 1 V. The piezoresistive sensitivity, $(\Delta I/I0)/\Delta P$, can be obtained by the linear slope of the plot, where SL and SH denote the sensitivity in the low and high pressure, respectively. ΔI is defined as IP – I0, in which IP is the measured current under certain pressure and I0 is the device current under minimum measurable pressure.

As shown in Figure 4a, for the vertical & micro-domes sensor, the current increases sharply in the pressure region below 2.5 kPa and yields a high sensitivity of 1428.3 kPa^{-1}, which is seven times higher than the random & micro-domes sensor of 196.3 kPa^{-1} and two times higher than the vertical & planar sensor of 680.9 kPa^{-1}. High piezoresistivity of the vertical & micro-domes sensor could be attributed to the alignment of mGN fillers. As discussed above, the fillers are getting closer to each other under pressure and form new conducting paths, leading to the increase in current. It is easier for mGN fillers aligned parallel to the loading direction to get close to each other and thus increasing the tunneling current, which is more likely to yield higher sensitivity of sensor than the one with random fillers, as shown in Figure 4d,f.

In addition to the contribution of fillers, the micro-dome structures of the sensor is easier to deform under the same pressure compared to the planar film. (14−16,52) Therefore, the contact area between the device and electrodes increases significantly, which decreases the contact resistance of the device and thus increases the current sharply. As shown in Figure 4a, the vertical & planar sensor shows much lower sensitivity than the one with micro-dome structures, which proves the contribution of sensor microstructures. It could be concluded that the superior high sensitivity of the vertical & micro-dome sensor results from two aspects, including the piezoresistivity caused by the increase in tunneling resistance among mGN fillers as well as the deformation of micro-dome structures under external pressure. As the loading further increases, there is a minimum distance among the fillers due to the physical

nonpenetration restriction and a saturation deformation of the device microstructure. As a result, the sensor sensitivity gradually decreases and gradually saturates in the region above 20 kPa.

To get more reliable results, five parallel vertical & micro-dome devices were fabricated and each device was continuously loaded four times to confirm the relative deviation among sensors (Figure S5). As displayed in Figure 4b, the average sensitivities of five sensors in low and high pressure range are 1302.1 and 40.6 kPa^{-1}, respectively. The device-to-device variations is low as 3.74% in the low pressure range and 9.09% in the high pressure range, lower than the common requirement of 10%, which proves the accuracy and precision of the mGN magnetic-assisted sensors. Figure 4c shows the current change of magnetic-assisted piezoresistive sensors under different loadings (72–128 Pa). The sensor exhibits a distinct current change under different pressures and even a subtle pressure change of 8 Pa could be sensed and recorded by the current change. Besides, the device can detect pressure as low as 72 Pa, which could meet the requirements for detecting pressure change resulted from very subtle motions and slight physiological signals like pulses.

To characterize the response speed of the sensor, a data acquisition (DAQ) card with a sampling rate of 500 Hz was used to record the voltage change of the sensor under pressure and the setup was shown in Figure 4g. Pressures at 10, 25, and 50 Hz were applied to the sensor by dynamic mechanical analysis (DMA). For 10, 25, and 50 Hz, the rise time of the sensor is 0.05, 0.02, and 0.01 s, respectively, which matches the frequency of loadings very well, proving the fast response of device even at a high frequency of 50 Hz (Figure 4h–j). Higher frequency test could not be performed because 50 Hz is the limit loading frequency of DMA equipment. Hence, the interval time from 10 to 90% of the full span at 50 Hz was defined as the actual response time of magnetic-assisted piezoresistive sensor, which is determined to be 6 ms, as shown in Figure 4j. Aside from high sensitivity and fast response, long-time stability is also very important for piezoresistive sensors. The magnetic-assisted piezoresistive sensor shows great durability and long-term stability after 20 000 loading and unloading

cycles at a frequency of 2 Hz. No obvious degradation could be observed after the cycle test, which contributed to the stability of mGN-EcoFlex composite (Figure S6).

Radial and Carotid Artery Pulse Monitoring

Cardiovascular diseases (CVDs) have been the top killer in the world and continuous monitoring of artery pulse, which is associated with hypertension, is of vital importance for the diagnosis and prevention of CVDs. (53,54) Therefore, in recent years, a lot of attention has been drawn to measure artery pulse objectively and automatically by wearable sensors with the advantages of high sensitivity, extreme thinness, ultralight weight, high flexibility, low cost, and great convenience. (6,7,14,55,56) In the following section, the proposed sensor was demonstrated in real-time human radial and carotid pulse measurements, followed by the evaluation of artery stiffness. Figure 5a,b exhibits human pulse waves of the radial artery and carotid artery measured by the magnetic-assisted piezoresistive sensor adhered to the neck of human and wrapped around the wrist in real-time.

As shown in Figure 5g, the typical radial artery pulse wave is composed of three waves. The first peak (P1) results from the ejection of the blood from the heart, which is reflected primarily at the aorta bifurcation. The reflection from the lower body is indicated by the second peak (P2). (55,57) P2/P1 is the radial artery augmentation index (AIr), which is a recognized parameter for evaluating arterial stiffness. (58,59) The stiffer the arteries, the quicker the pulse wave travels through the vessel and the earlier the reflected wave arrives in P1, which will increase the AIr and decrease the time interval between peaks P1 and P2 (ΔT_{DVP}). Therefore, the increase of AIr indicates a reduced arterial elasticity, usually associated with aging, hypertension, or arteriosclerosis. (59,60) The regular and stable waves of a normal healthy person and the values of ΔT_{DVP} = 0.26 s and AIr = 0.49 in Figure 5e,f are consistent with the expected results for healthy 26-year-old adults. (60)

Human Motion Sensing

To demonstrate the potential application in detecting human motions, the sensor was

applied to sense the subtle human motions, such as facial expressions, finger gestures, and phonations. The sensor was fixed on the skin surface and connected to a Keithley 2602 source meter to continuously record the current responses to the motions. As shown in Figure 6a, the piezoresistive sensor could be used to monitor the microexpressions since different facial expressions would generate different levels of current increase, which resulted from the decrease of distances among fillers and the increase of the contact area between the device microstructure and electrode. The sensor was then fixed on the surface of an index finger to monitor finger gestures, as shown in Figure 6b,c. Once the finger is bent, the pressure is generated and the current of the sensor increases. When the finger is bent slightly and dramatically, the current responses are clearly different and could be easily distinguished, thus realizing the monitoring of finger gestures. Figure 6b displays current responses of a gesture repeated tens of times and Figure 6c shows continuous responses by holding the finger in different bending states for a few seconds. Finally, the sensor was adhered on Adam's apple to sense different human phonations. Different phonations result in different levels of pressures to the sensor, reflected by the measured currents in Figure 6d–f. For example, "bad" with two syllables will generate two main peaks in the current response curve, and three syllables like "wonderful" will yield three. It can be seen that different phonations could be identified easily. Moreover, the current of the sensor shows stable and repetitive signals, proving excellent stability and repeatability of the sensor in body motion sensing applications.

Conclusions

In summary, mGN hybrids were synthesized and mixed with EcoFlex matrix to achieve the transparent conductive mGN-EcoFlex film. A low percolation threshold of 0.27% was achieved owing to the large excluded volume and controllable alignment of mGN fillers, which lead to the electrical conductivity of 0.003 S m^{-1}, a transmittance of 71.8%, and low Young's modulus of 122.8 kPa. This micro-dome-shaped mGN-EcoFlex composite was used to replace the two-layer structure to address the problem of Young's modulus mismatch. It is noted that the

microstructure was derived from the template prepared by hot embossing technology, which could generate a regular micro-dome array with controllable size and density cost-effectively. Magnetic-assisted and micro-dome structured piezoresistive sensors were fabricated with vertically aligned mGN fillers, which exhibit superior sensitivity of 1302.1 kPa^{-1}. The magnetic-assisted sensor shows great potential in next-generation wearable devices for real-time human health monitoring, such as detecting human artery pulses and monitoring human motions.

Author Information

Corresponding Authors

Zongrong Wang - State Key Lab of Silicon Materials, School of Materials Science and Engineering, Zhejiang University, Hangzhou 310027, China; http://orcid.org/0000-0003-4588-8640; Email: zrw@zju.edu.cn

Hongzhu Wang - Department of Equipment Division, Women's Hospital, School of Medicine, Zhejiang University, Hangzhou 310027, China; Email: lib@zju.edu.cn

Chi Wah Leung - Department of Applied Physics, The Hong Kong Polytechnic University, Hung Hom, Hong Kong 999077, China; Email: apleung@polyu.edu.hk

Shaoxing Qu - State Key Laboratory of Fluid Power & Mechatronic System, Key Laboratory of Soft Machines and Smart Devices of Zhejiang Province, Center for X-Mechanics, and Department of Engineering Mechanics, Zhejiang University, Hangzhou 310027, China; Email: squ@zju.edu.cn

Authors

Shan Wang - State Key Lab of Silicon Materials, School of Materials Science and Engineering, Zhejiang University, Hangzhou 310027, China

Guorui Chen - State Key Lab of Silicon Materials, School of Materials Science and Engineering, Zhejiang University, Hangzhou 310027, China

Shaoyu Niu - State Key Lab of Silicon Materials, School of Materials Science and

Engineering, Zhejiang University, Hangzhou 310027, China

Kaifeng Chen - State Key Lab of Silicon Materials, School of Materials Science and Engineering, Zhejiang University, Hangzhou 310027, China

Tian Gan - State Key Lab of Silicon Materials, School of Materials Science and Engineering, Zhejiang University, Hangzhou 310027, China

Piyi Du - State Key Lab of Silicon Materials, School of Materials Science and Engineering, Zhejiang University, Hangzhou 310027, China

Notes

The authors declare no competing financial interest.

Acknowledgments

This work was supported by the Zhejiang Provincial Natural Science Foundation (Grant number LY17F040003), the National Natural Science Foundation of China (Grant numbers 51702285, 91748209, 11525210, and 11621062), and Zhejiang Medical and Health Science and Technology Plan Project (2018PY014). The authors also thank the support of HKSAR PolyU 153027/17P(RGC) and 1-ZVGH(PolyU).

Figures

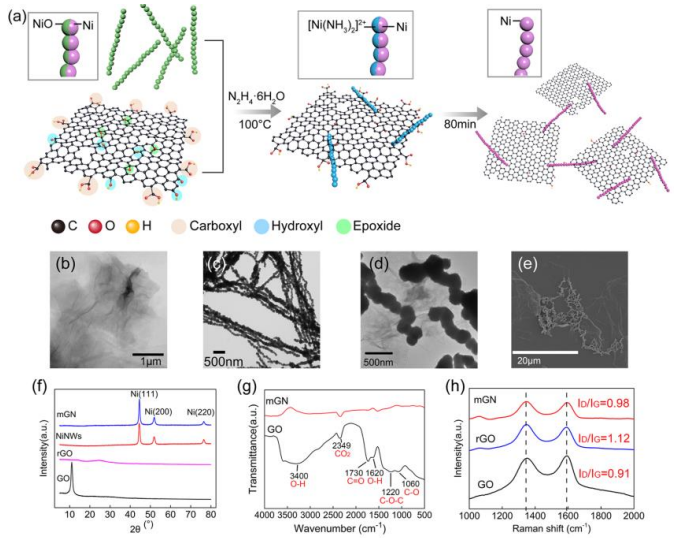

Figure 1. (a) Schematic diagram of mGN hybrids formation. (b) TEM image of GO. (c) TEM image of NiNWs. (d) TEM and (e) SEM images of mGN hybrids, respectively. (f) X-ray diffraction (XRD) patterns of GO, rGO, NiNWs, and mGN hybrids, respectively. (g) Fourier transform infrared (FTIR) spectra of GO and mGN hybrids, respectively. (h) Raman spectra of GO, rGO, and mGN hybrids, respectively.

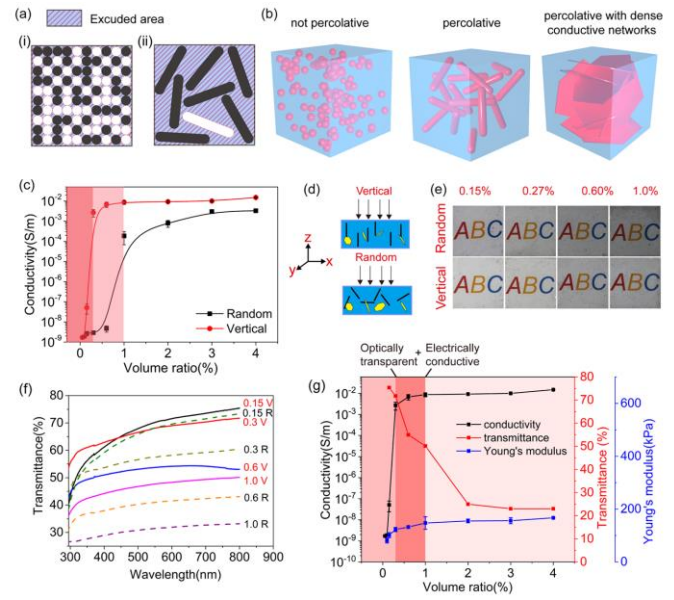

Figure 2. (a) Two-dimensional (2D) schematic diagram of the excluded area. (i) Fifty spheres dispersed randomly in a square. (ii) Seven rods dispersed in the same square and the total area is approximately the same with 50 spheres. (b) Spheres, rods, and disks with the same total volume are dispersed in the same cubic. (c) The conductivity of mGN-EcoFlex composite films with mGN

distributed randomly and vertically as a function of volume ratio, respectively. (d) Schematic diagram of the light transmission in films with randomly and vertically aligned mGN. (e) Optical photographs of mGN-EcoFlex films with different volume ratios and the alignment direction of fillers. (f) Transmittance of mGN-EcoFlex films with different volume ratio and alignment of fillers, where R and V represent random and vertical, respectively. (g) Conductivity, transmittance, and Young's modulus of mGN-EcoFlex films with vertically aligned mGN as a function of volume ratio.

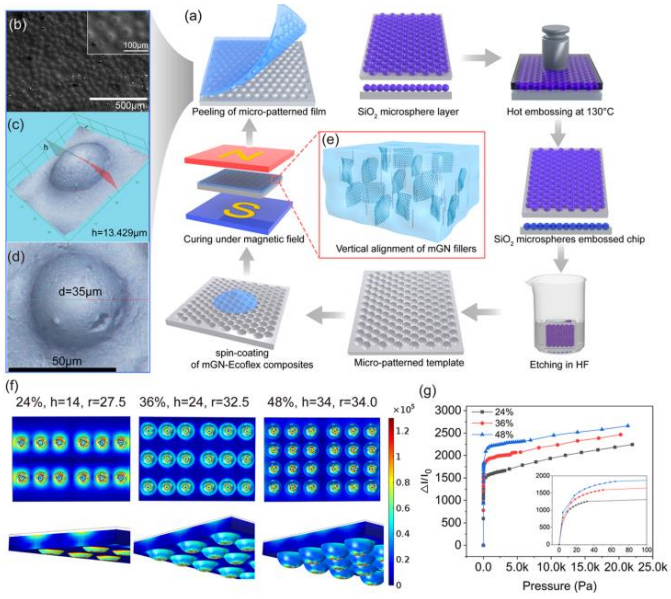

Figure 3. (a) Schematic diagram of fabricating micro-dome templates by hot embossing technology and micro-patterned mGN-EcoFlex film with vertically aligned mGN hybrids. (b) SEM image of mGN-EcoFlex film molded from the template. (c) Three-dimensional (3D) image of mGN-EcoFlex film from a perspective view. (d) Three-dimensional (3D) image of mGN-EcoFlex film from the top view. (e) Schematic illustration of mGN-EcoFlex film with mGN fillers aligned vertically. (f) Surface Von Mises stress of pressure sensors with different density and height of micro-domes. (g) Simulation results of $\Delta I/I0$ versus pressure. Inset is the zoomed-in figure of $\Delta I/I0$ versus pressure (0–100 Pa).

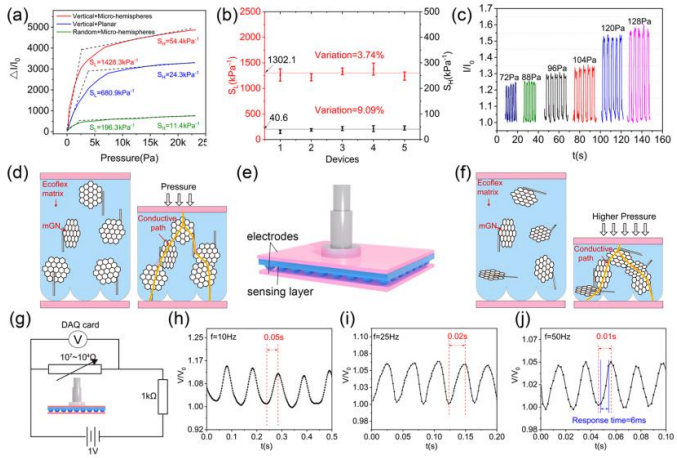

Figure 4. (a) Representative current response curve versus pressure of vertical & micro-domes, random & micro-domes, and vertical & planar sensor. (b) Histogram of sensitivities in low and high pressure range of five parallel sensors, respectively. (c) Current change of magnetic-assisted piezoresistive sensor under different loadings (72–128 Pa). (d) Sensing mechanism of vertical & micro-domes sensor under pressure. (e) Schematic diagram of the loading setup. Continuous loadings generated by the force gauge were applied to the sensor through a silicon wafer with an area of 5 mm × 5 mm. (f) Sensing mechanism of random & micro-domes sensor under pressure. (g) The circuit diagram of the measurement setup for a frequency response of the piezoresistive sensor. (h, i, j) Voltage outputs of the sensor at different loading frequencies of 10, 25, and 50 Hz.

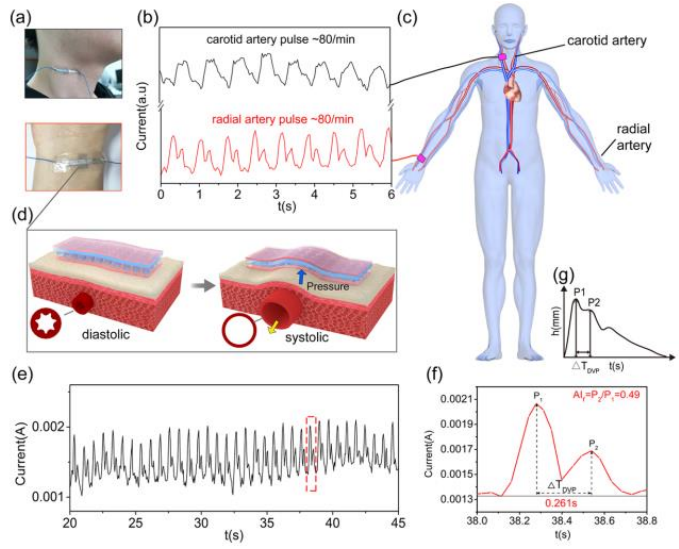

Figure 5. Human pulse waves of the radial artery and carotid artery measured by a magnetic-assisted piezoresistive sensor. (a) Photographs of the piezoresistive sensor adhered to the

neck and wrapped around the wrist. (b) Carotid and radial artery pulse waves measured in real-time by the sensor. (c) Schematic of vascular distribution in the human body. (d) Schematic diagram of the artery changes during systole and diastole processes and sensing process by the sensor. (e) Real-time transient signal of radial artery pulse wave for 25 s. (f) Zoomed-in view of a single radial artery pulse shown as dotted rectangular in (e) to assess the artery health. (g) Typical human radial artery pulse.

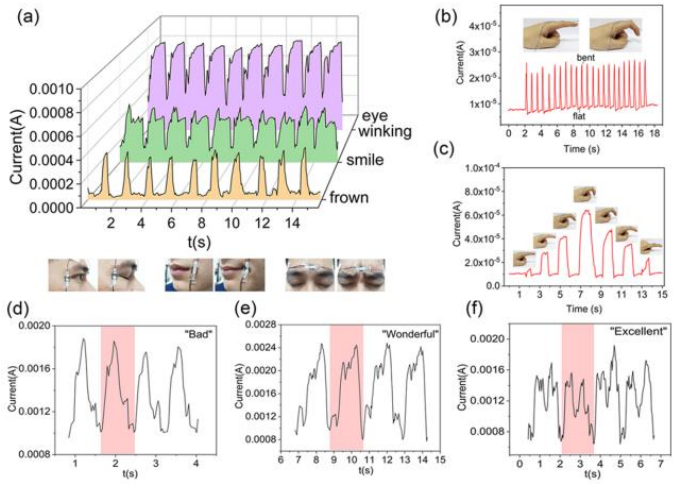

Figure 6. Demonstrations of the piezoresistive sensor on human motion sensing. (a) Current responses to different facial expressions, including eye winking, smile, and frown. (b) Current response of the sensor for a finger gesture in bending–flat–bending cycles. (c) Continuous response of the current with different finger gestures. Current responses of the piezoresistive sensor associated with different phonations, including (d) bad, (e) wonderful, and (f) “Excellent”.

References

(1) Bae, G. Y.; Han, J. T.; Lee, G.; Lee, S.; Kim, S. W.; Park, S.; Kwon, J.; Jung, S.; Cho, K. Pressure/Temperature Sensing Bimodal Electronic Skin with Stimulus Discriminability and Linear Sensitivity. Adv. Mater. 2018, 30, No. 1803388.

(2) Lai, Y. C.; Deng, J.; Liu, R.; Hsiao, Y. C.; Zhang, S. L.; Peng, W.; Wu, H. M.; Wang, X.; Wang, Z. L. Actively Perceiving and Responsive Soft Robots Enabled by Self-Powered, Highly Extensible, and Highly Sensitive Triboelectric Proximity- and Pressure-Sensing Skins. Adv. Mater. 2018, 30, No. 1801114.

(3) Chen, S.; Song, Yj.; Ding, D.; Ling, Z.; Xu, F. Flexible and Anisotropic Strain Sensor Based on Carbonized Crepe Paper with Aligned Cellulose Fibers. Adv. Funct. Mater. 2018, 28, No. 1802547.

(4) You, I.; Choi, S. E.; Hwang, H.; Han, S. W.; Kim, J. W.; Jeong, U. E-Skin Tactile Sensor Matrix Pixelated by Position-Registered Conductive Microparticles Creating Pressure-Sensitive Selectors. Adv. Funct. Mater. 2018, 28, No. 1801858.

(5) Dahiya, R. S.; Metta, G.; Valle, M.; Sandini, G. Tactile SensingFrom Humans to Humanoids. IEEE Trans. Rob. 2010, 26, 1−20.

(6) Boutry, C. M.; Nguyen, A.; Lawal, Q. O.; Chortos, A.; Rondeaugagne, S.; Bao, Z. A Sensitive and Biodegradable Pressure´ Sensor Array for Cardiovascular Monitoring. Adv. Mater. 2015, 27, 6953−6960.

(7) Huang, C. B.; Witomska, S.; Aliprandi, A.; Stoeckel, M. A.; Bonini, M.; Ciesielski, A.; Samori, P. Molecule-Graphene Hybrid Materials with Tunable Mechanoresponse: Highly Sensitive Pressure Sensors for Health Monitoring. Adv. Mater. 2019, 31, No. 1804600.

(8) Shi, J.; Wang, L.; Dai, Z.; Zhao, L.; Du, M.; Li, H.; Fang, Y. Multiscale Hierarchical Design of a Flexible Piezoresistive Pressure Sensor with High Sensitivity and Wide Linearity Range. Small 2018, 14, No. 1800819.

(9) Shi, X.; Liu, S.; Sun, Y.; Liang, J.; Chen, Y. Lowering Internal Friction of 0D-1D-2D Ternary Nanocomposite-Based Strain Sensor by Fullerene to Boost the Sensing Performance. Adv. Funct. Mater. 2018, 28, No. 1800850.

(10) Zhang, L.; Chen, K.; Wang, S.; Chen, S.; Niu, S.; Wang, Z.; Du, P. Synthesis of Percolative Hyperelastic Conducting Composite and Demonstrations of Application in Wearable Strain Sensors. Mater. Lett. 2018, 233, 306−309.

(11) Charara, M.; Abshirini, M.; Saha, M. C.; Altan, M. C.; Liu, Y. Highly Sensitive Compression Sensors Using Three-dimensional Printed Polydimethylsiloxane/carbon Nanotube Nanocomposites. J. Intell. Mater. Syst. Struct. 2019, 30, 1216−1224.

(12) Chowdhury, S. A.; Saha, M. C.; Patterson, S.; Robison, T.; Liu, Y. Highly Conductive Polydimethylsiloxane/Carbon Nanofiber Composites for Flexible Sensor Applications. Adv. Mater. Technol. 2019, 4, No. 1800398.

(13) Wei, Z.; Zhou, Z. K.; Li, Q.; Xue, J.; Di, F. A.; Yang, Z.; Zhou, J.; Wang, X. Flexible Nanowire Cluster as a Wearable Colorimetric Humidity Sensor. Small 2017, 13, No. 1700109.

(14) Choong, C. L.; Shim, M. B.; Lee, B. S.; Jeon, S.; Ko, D. S.; Kang, T. H.; Bae, J.; Lee, S. H.; Byun, K. E.; Im, J.; Jeong, Y. J.; Park, C. E.; Park, J. J.; Chung, U. I. Highly Stretchable Resistive Pressure Sensors Using a Conductive Elastomeric Composite on a Micropyramid Array. Adv. Mater. 2014, 26, 3451−3458.

(15) Wang, Z.; Wang, S.; Zeng, J.; Ren, X.; Chee, A. J.; Yiu, B. Y.; Chung, W. C.; Yang, Y.; Yu, A. C.; Roberts, R. C.; Tsang, A. C.; Chow, K. W.; Chan, P. K. High Sensitivity, Wearable, Piezoresistive Pressure Sensors Based on Irregular Microhump Structures and Its Applications in Body Motion Sensing. Small 2016, 12, 3827−3836.

(16) Pang, Y.; Zhang, K.; Yang, Z.; Jiang, S.; Ju, Z.; Li, Y.; Wang, X.; Wang, D.; Jian, M.; Zhang, Y.; Liang, R.; Tian, H.; Yang, Y.; Ren, T.- L. Epidermis Microstructure Inspired Graphene Pressure Sensor with Random Distributed Spinosum for High Sensitivity and Large Linearity. ACS Nano 2018, 12, 2346−2354.

(17) Zhu, B.; Niu, Z.; Wang, H.; Leow, W. R.; Wang, H.; Li, Y.; Zheng, L.; Wei, J.; Huo, F.; Chen, X. Microstructured Graphene Arrays for Highly Sensitive Flexible Tactile Sensors. Small 2014, 10, 3625−3631.

(18) Wang, X.; Gu, Y.; Xiong, Z.; Cui, Z.; Zhang, T. Silk-Molded Flexible, Ultrasensitive, and Highly Stable Electronic Skin for Monitoring Human Physiological Signals. Adv. Mater. 2014, 26, 1336−1342.

(19) Su, B.; Gong, S.; Ma, Z.; Yap, L. W.; Cheng, W. Mimosainspired Design of a Flexible Pressure Sensor with Touch Sensitivity. Small 2015, 11, 1886−1891.

(20) Fan, F. R.; Lin, L.; Zhu, G.; Wu, W.; Zhang, R.; Wang, Z. L. Transparent Triboelectric Nanogenerators and Self-powered Pressure Sensors based on Micropatterned Plastic Films. Nano Lett. 2012, 12, 3109−3114.

(21) Wang, Z.; Volinsky, A. A.; Gallant, N. D. Crosslinking Effect on Polydimethylsiloxane Elastic Modulus Measured by Custom-built Compression Instrument. J. Appl. Polym. Sci. 2015, 131, No. 41050.

(22) Lipomi, D. J.; Lee, J. A.; Vosgueritchian, M.; Tee, B. C. K.; Bolander, J. A.; Bao, Z. Electronic Properties of Transparent Conductive Films of PEDOT:PSS on Stretchable Substrates. Chem. Mater. 2012, 24, 373−382.

(23) Strümpler, R.; Glatz-Reichenbach, J. Conducting Polymer Composites. J. Electroceram. 1999, 3, 329−346.

(24) Huang, X.; Zhi, C. Polymer Nanocomposites: Electrical and Thermal Properties; Springer, 2016.

(25) Su, J.; Mirzaee, I.; Gao, F.; Liu, X.; Charmchi, M.; Gu, Z.; Sun, H. Magnetically Assembling Nanoscale Metal Network Into Phase Change Material-Percolation Threshold Reduction in Paraffin Using Magnetically Assembly of Nanowires. J. Nanotechnol. Eng. Med. 2014, 5, No. 031005.

(26) Yang, B.; Liu, G.; Han, S.; Cao, W.; Chen, H.; Lu, J.; Shieh, H. D. Hybrid Effect of Crossed Alignment and Multi-Stacking Structure on the Percolation Behavior of Silver Nanowire Networks. J. Disp. Technol. 2015, 11, 625−629.

(27) Wang, Y.; Shan, J. W.; Weng, G. J. Percolation Threshold and Electrical Conductivity of Graphene-based Nanocomposites with Filler Agglomeration and Interfacial Tunneling. J. Appl. Phys. 2015, 118, No. 065101.

(28) Ci, L.; Suhr, J.; Pushparaj, V.; Zhang, X.; Ajayan, P. M. Continuous Carbon Nanotube Reinforced Composites. Nano Lett. 2008, 8, 2762−2766.

(29) Choi, S.; Han, S. I.; Kim, D.; Hyeon, T.; Kim, D.-H. Highperformance Stretchable Conductive Nanocomposites: Materials, Processes, and Device Applications. Chem. Soc. Rev. 2019, 48, 1566−1595.

(30) Lipomi, D. J.; Vosgueritchian, M.; Tee, B. C.-K.; Hellstrom, S. L.; Lee, J. A.; Fox, C. H.; Bao, Z. Skin-like Pressure and Strain Sensors Based on Transparent Elastic Films of Carbon Nanotubes. Nat. Nanotechnol. 2011, 6, 788−792.

(31) Lim, S.; Son, D.; Kim, J.; Lee, Y. B.; Song, J. K.; Choi, S.; Lee, D. J.; Kim, J. H.; Lee, M.; Hyeon, T.; Kim, D.-H. Transparent and Stretchable Interactive Human Machine Interface Based on Patterned Graphene Heterostructures. Adv. Funct. Mater. 2015, 25, 375−383.

(32) Balberg, I.; Anderson, C. H.; Alexander, S.; Wagner, N. Excluded Volume and its Relation to the Onset of Percolation. Phys. Rev. B 1984, 30, 3933−3943.

(33) Celzard, A.; Mcrae, E.; Deleuze, C.; Dufort, M.; Furdin, G.; Marê che, J. F. Critical Concentration in Percolating Systems′ Containing a High-aspect-ratio Filler. Phys. Rev. B 1996, 53, 6209− 6214.

(34) Philipse, A. P. The Random Contact Equation and Its Implications for Colloid Rods in Packings, Suspensions, and Anisotropic Powders. Langmuir 1996, 12, 1127−1133. (35) Shao, Q.; Niu, Z.; Hirtz, M.; Jiang, L.; Liu, Y.; Wang, Z.; Chen, X. High-Performance and Tailorable Pressure Sensor Based on Ultrathin Conductive Polymer Film. Small 2014, 10, 1466−1472.

(36) Yang, X.; Zhang, X.; Ma, Y.; Huang, Y.; Wang, Y.; Chen, Y. Superparamagnetic Graphene Oxide-Fe3O4 Nanoparticles Hybrid for Controlled Targeted Drug Carriers. J. Mater. Chem. 2009, 19, 2710− 2714.

(37) Zhao, C.; Guo, J.; Yang, Q.; Tong, L.; Zhang, J.; Zhang, J.; Gong, C.; Zhou, J.; Zhang, Z. Preparation of Magnetic Ni@graphene Nanocomposites and Efficient Removal Organic Dye under Assistance of Ultrasound. Appl. Surf. Sci. 2015, 357, 22−30.

(38) Wang, L.; Ma, F.; Shi, Q.; Liu, H.; Wang, X. Study on Compressive Resistance Creep and Recovery of Flexible Pressure Sensitive Material Based on Carbon Black Filled Silicone Rubber Composite. Sens. Actuators, A 2011, 165, 207−215.

(39) How, G. T. S.; Pandikumar, A.; Ming, H. N.; Ngee, L. H. Highly Exposed {001} Facets of Titanium Dioxide Modified with Reduced Graphene Oxide for Dopamine Sensing. Sci. Rep. 2014, 4, No. 5044.

(40) Guo, J.; Wang, R.; Weng, W. T.; Pan, J.; Liu, T. Synthesis of Fe Nanoparticles@graphene Composites for Environmental Applications. J. Hazard. Mater. 2012, 225−226, 63−73.

(41) Moon, I. K.; Lee, J.; Ruoff, R. S.; Lee, H. Reduced Graphene Oxide by Chemical Graphitization. Nat. Commun. 2010, 1, No. 73.

(42) Aviles, F.; Oliva-Avile´ s, A. I.; Cen-Puc, M. Piezoresistivity,´ Strain, and Damage Self-Sensing of Polymer Composites Filled with Carbon Nanostructures. Adv. Eng. Mater. 2018, 20, No. 1701159.

(43) Gao, J.; Huang, H.; Yan, D.; Ren, P.; Zeng, X.; Li, Z. Resistivity Relaxation of Anisotropic Conductive Polymer Composites. J. Macromol. Sci., Part B: Phys. 2013, 52, 788−796.

(44) Oliva-Aviles, A. I.; Avile´ s, F.; Sosa, V. Electrical and´ Piezoresistive Properties of Multi-walled Carbon Nanotube/polymer Composite Films Aligned by an Electric Field. Carbon 2011, 49, 2989−2997.

(45) Hangarter, C. M.; Myung, N. V. Magnetic Alignment of Nanowires. Chem. Mater. 2005, 17, 1320−1324.

(46) Tanase, M.; Bauer, L. A.; Hultgren, A.; Silevitch, D. M.; Sun, L.; Reich, D. H.; Searson, P. C.; Meyer, G. J. Magnetic Alignment of Fluorescent Nanowires. Nano Lett. 2001, 1, 155−158.

(47) Silver, F.; Freeman, J.; Devore, D. Viscoelastic Properties of Human Skin and Processed Dermis. Skin Res. Technol. 2001, 7, 18− 23.

(48) Joodaki, H.; Panzer, M. B. Skin Mechanical Properties and Modeling: A review. Proc. Inst. Mech. Eng., Part H 2018, 232, 323− 343.

(49) Zetina-Hernandez, O.; Duarte-Aranda, S.; May-Pat, A.;´ Canche-Escamilla, G.; Uribe-Calderon, J.; Gonzalez-Chi, P. I.;´ Aviles, F. Coupled Electro-mechanical Properties of Multiwall Carbon´ Nanotube/polypropylene Composites for Strain Sensing Applications. J. Mater. Sci. 2013, 48, 7587−7593.

(50) Alamusi; Hu, N.; Fukunaga, H.; Atobe, S.; Liu, Y.; Li, J. Piezoresistive Strain Sensors Made from Carbon Nanotubes Based Polymer Nanocomposites. Sensors 2011, 11, 10691−10723.

(51) Hu, N.; Karube, Y.; Yan, C.; Masuda, Z.; Fukunaga, H. Tunneling Effect in a Polymer/carbon Nanotube Nanocomposite Strain Sensor. Acta Mater. 2008, 56, 2929−2936.

(52) Park, J.; Lee, Y.; Hong, J.; Ha, M.; Jung, Y. D.; Lim, H.; Kim, S. Y.; Ko, H. Giant Tunneling Piezoresistance of Composite Elastomers with Interlocked Microdome Arrays for Ultrasensitive and Multimodal Electronic Skins. ACS Nano 2014, 8, 4689−4697.

(53) Kannel, W. B. Blood Pressure as a Cardiovascular Risk Factor: Prevention and Treatment. JAMA 1996, 275, 1571−1576.

(54) Kannel, W. B. Diabetes and Cardiovascular Disease: The Framingham Study. JAMA 1979, 241, 2035−2038.

(55) Schwartz, G.; Tee, B. C.; Mei, J.; Appleton, A. L.; Kim, D. H.; Wang, H.; Bao, Z. Flexible Polymer Transistors with High Pressure Sensitivity for Application in Electronic Skin and Health Monitoring. Nat. Commun. 2013, 4, No. 1859.

(56) Pang, C.; Koo, J. H.; Nguyen, A.; Caves, J. M.; Kim, M. G.; Chortos, A.; Kim, K.; Wang, P. J.; Tok, J. B.; Bao, Z. Highly Skinconformal Microhairy Sensor for Pulse Signal Amplification. Adv. Mater. 2015, 27, 634−640.

(57) Qiao, L.-j.; Qi, Z.; Tu, L.-p.; Zhang, Y.-h.; Zhu, L.-p.; Xu, J.-t.; Zhang, Z.-f. The Association of Radial Artery Pulse Wave Variables with the Pulse Wave Velocity and Echocardiographic Parameters in Hypertension. J. Evidence-Based Complementary Altern. Med. 2018, 2018, No. 5291759.

(58) Fan, X.; Huang, Y.; Ding, X.; Luo, N.; Li, C.; Zhao, N.; Chen, S. Alignment-Free Liquid-Capsule Pressure Sensor for Cardiovascular Monitoring. Adv. Funct. Mater. 2018, 28, No. 1805045.

(59) Millasseau, S. C.; Patel, S. J.; Redwood, S. R.; Ritter, J. M.; Chowienczyk, P. J. Pressure Wave Reflection Assessed from the Peripheral Pulse: Is a Transfer Function Necessary? Hypertension 2003, 41, 1016−1020.

(60) Nichols, W. W. Clinical Measurement of Arterial Stiffness Obtained from Noninvasive Pressure Waveforms. Am. J. Hypertens. 2005, 18, 3−10.